PHYSICAL REVIEW APPLIED **23,** 024039 (2025)

Editors' Suggestion

Interface states in two-dimensional quasicrystals with broken inversion symmetry

Danilo Beli,[1,*] Matheus I.N. Rosa,[2] Luca Lomazzi,[3] Carlos De Marqui, Jr.,[1] and
Massimo Ruzzene[2]

[1] *Department of Aeronautical Engineering, São Carlos School of Engineering, University of São Paulo, Brazil*
[2] *Department of Mechanical Engineering, College of Engineering and Applied Science,*
University of Colorado Boulder, USA
[3] *Department of Mechanical Engineering, Politecnico di Milano, Milano, Italy*

(Received 7 March 2024; revised 23 December 2024; accepted 6 January 2025; published 18 February 2025)

We investigate the existence of interface states induced by broken inversion symmetries in two-dimensional quasicrystal (QC) lattices. We introduce a 10-fold rotationally symmetric QC lattice whose inversion symmetry is broken through a mass dimerization that produces two fivefold symmetric sublattices. By considering resonator scatterers attached to an elastic plate, we illustrate the emergence of bands of interface states that accompany a band inversion of the QC spectrum as a function of the dimerization parameter. These bands are filled by modes which are localized along domain wall interfaces separating regions of opposite inversion symmetry. These features draw parallels to the dynamic behavior of topological interface states in the context of the valley Hall effect, which has so far been limited to periodic lattices. We numerically and experimentally demonstrate waveguiding in a QC lattice featuring a zigzag interface with sharp turns of 36°, which goes beyond the limitation of 60° associated with sixfold symmetric (i.e., honeycomb) periodic lattices. Our results provide new opportunities for symmetry-based quasicrystalline topological waveguides that do not require time-reversal symmetry breaking, and that allow for higher freedom in the design of their waveguiding trajectories by leveraging higher-order rotational symmetries.

DOI: 10.1103/PhysRevApplied.23.024039

I. INTRODUCTION

The discovery of topological insulators [1] has opened up opportunities for robust wave localization and transport across multiple disciplines, including through classical waves by leveraging photonic [2,3], acoustic [4,5], and elastic metamaterials [6,7]. The examples realized so far illustrate a wealth of strategies for the design of backscattering-free waveguides with a high degree of immunity to defects, a feature deemed promising for technological applications and devices. Typically, these phenomena are unlocked by engineering the band structure of periodic lattices, for example by nucleating degeneracies and opening band gaps through the careful manipulation and selective breaking of their symmetries. A current challenge has been to extend these concepts to aperiodic and disordered materials in general. For example, edge states originally attributed to the quantum Hall effect (QHE) [8,9] have been observed to persist in amorphous gyroscopic lattices [10]. Other studies have considered quasiperiodic lattices of effective extended dimensionalities by leveraging additional dimensions established in their parameter spaces [11,12]. Under this framework, edge states reminiscent of the two-dimensional (2D) QHE have been realized in 1D quasiperiodic lattices [13–21], while those reminiscent of the 4D QHE have been realized in 2D quasiperiodic lattices [22–24].

In this context, there has been significant interest in exploring the existence of topological states in quasicrystals (QCs). While they lack translational periodicity, QCs have long-range order [25,26] and form a particularly interesting class of aperiodic lattices since they may exhibit spatial symmetries which are forbidden in periodic crystals, such as 5-, 7-, 8-, and 10-fold rotational symmetries in the plane, and, for example, icosahedral symmetries in three dimensions [27]. The interplay between their unique symmetries and the concepts of topological physics is a subject of ongoing investigations [28,29], which may lead to unprecedented phenomena. Some studies have demonstrated the existence of edge states reminiscent of the QHE in 2D QCs, for example in quantum lattices subject to an external magnetic field [30–32] and photonic lattices with artificial gauge fields [33]. The existence of higher-order topological corner states has also been demonstrated in quantum QC lattices [34,35]. In passive materials, which preserve time-reversal symmetry, implementations are more scarce since they must solely

---

[*] Contact author: beli.danilo@gmail.com

rely on the manipulation of their real-space symmetries. One example is the observation of topological boundary floppy modes in elastic Maxwell QC lattices [36], which extends the behavior previously observed in periodic lattices [37] to the orientation symmetries of QCs, but limited to zero frequency. Another example is the extension of the spin Hall effect (SHE) [38] to QC quantum lattices with spin-orbit coupling [39,40]. While theoretically proposed, an experimental realization is still missing, perhaps due to the challenges associated with synthesizing atomic-scale QCs. In addition, the observation of the SHE in the context of classical waves is already intricate in the periodic case, where pseudospin degrees of freedom are generated through the careful nucleation and lifting of a double Dirac degeneracy [2,41–45]. The absence of translational periodicity and Bloch-Floquet dispersion analysis makes the introduction of such pseudospin features in QCs very challenging, and, therefore, the extension of the SHE to classical QCs is still missing.

Here we investigate the existence of interface states in passive 2D QC lattices induced solely by inversion symmetry breaking. Our approach is inspired by the valley Hall effect (VHE) [46,47], which is typically achieved by breaking the inversion symmetry of periodic sixfold rotationally symmetric lattices (i.e., honeycomb lattices). This framework is more straightforward than intricate designs to emulate pseudospin effects and provides one of the simplest avenues towards topological states in passive 2D materials, as evidenced by numerous classical wave implementations [48–55]. However, approaches based on inversion symmetry breaking have been scarcely applied to QC lattices, with current examples limited to 1D waveguides supporting interface states [16,56]. We illustrate the phenomenon using a 10-fold rotationally symmetric QC lattice whose broken inversion symmetry is achieved through a dimerization that produces two fivefold symmetric sublattices (Fig. 1). By considering resonators attached to an elastic plate, our simulations uncover features analogous to those observed in the context of the VHE for periodic lattices. These include a band inversion as a function of the dimerization parameter, and the appearance of interface states localized along domain walls that separate two regions of opposite inversion symmetry. We also exploit the interface states to create waveguides with sharp angular turns of 36°, which goes beyond the 60° limitation associated with the orientation of sixfold periodic lattice vectors. Finally, the simplicity of the proposed framework, based solely on inversion symmetry breaking, allow us to experimentally demonstrate these features on a macroscopic additive manufactured elastic plate.

This paper is organized as follows. Section II introduces the design methodology for the dimerized QC lattices, and the implementation using elastic resonators. Section III then describes the spectral properties uncovered by numerical simulations, while Sec. IV provides the results of experimental investigations. Finally, Sec. V summarizes the key findings of this study and outlines future research directions.

II. DESIGN OF DIMERIZED QUASICRYSTAL LATTICES WITH BROKEN INVERSION SYMMETRY

The QC lattices considered are obtained through the discretization of continuous fields that exhibit the desired rotational symmetry (Fig. 1). A continuous field in physical space $\phi(\mathbf{r})$, with $\mathbf{r} = [x, y] \in \mathcal{R}^2$, is defined by directly assigning N rotationally symmetric peaks in reciprocal space ($\boldsymbol{\kappa} = [\kappa_x, \kappa_y] \in \mathcal{R}^2$) as points in the 2D Fourier spectra [57,58]. These peaks are angularly spaced by $\theta_N = 2\pi/N$ over a circle of fundamental wave number $\kappa_0 = 2\pi/\lambda_0$, where λ_0 is the fundamental wavelength. Therefore, physical and reciprocal spaces can be expressed as

$$\phi(\mathbf{r}) = \sum_{n=0}^{N-1} e^{i(\kappa_n\cdot\mathbf{r}+\phi_n)}, \quad \hat{\phi}(\boldsymbol{\kappa}) = \sum_{n=0}^{N-1} e^{i\phi_n}\delta(\boldsymbol{\kappa}-\boldsymbol{\kappa}_n), \tag{1}$$

where δ is the delta function that locates the wave number $\boldsymbol{\kappa}_n = \kappa_0[\cos(n\theta_N), \sin(n\theta_N)]$ of the nth peak, with phase ϕ_n. This procedure traditionally employs even N and zero phases ($\phi_n = 0$) to produce real fields with C_N symmetry (i.e., N-fold rotational symmetry), including crystalline (periodic) distributions, such as square and hexagonal fields with C_4 and C_6 symmetries, and quasicrystalline (quasiperiodic) distributions, such as C_8 and C_{10} QCs [59,60]. In such cases, there are $N/2$ pairs of diametrically opposite peaks of equal phases in the reciprocal space circle, and each pair defines one cosine function. The superposition of these $N/2$ cosines, which are even functions, defines a field with C_N symmetry. Here we introduce the phase term $\phi_n = n\pi + \pi/2$ to break the inversion symmetry of $\phi(\mathbf{r})$, replacing C_N symmetry by $C_{N/2}$ symmetry due to alternating phases of $\pi/2$ and $-\pi/2$ for subsequent peaks along the circle. This can equivalently be interpreted as replacing each of the $N/2$ cosine functions described above by sinusoidal ones, which are odd functions. An example of a quasicrystalline field with C_5 symmetry obtained with $N = 10$ is shown in the left panel of Fig. 1(a), with the inset illustrating the Fourier peaks of alternating phases. Notice that the overall field structure resembles the C_{10} symmetric case [59,60], but the alternating blue and red colors indicate that inversion symmetry was broken as there are no remaining lines of mirror symmetry, and therefore only C_5 symmetry is preserved. Similarly, the usage of $N = 6$ produces a field which breaks C_6 symmetry into C_3 symmetry, also eliminating the mirror (inversion) symmetry of the former case. Further details on such design procedure are given in Appendix A, including the periodic $C_6 \rightarrow C_3$ case, and another quasicrystalline $C_{14} \rightarrow C_7$ example.

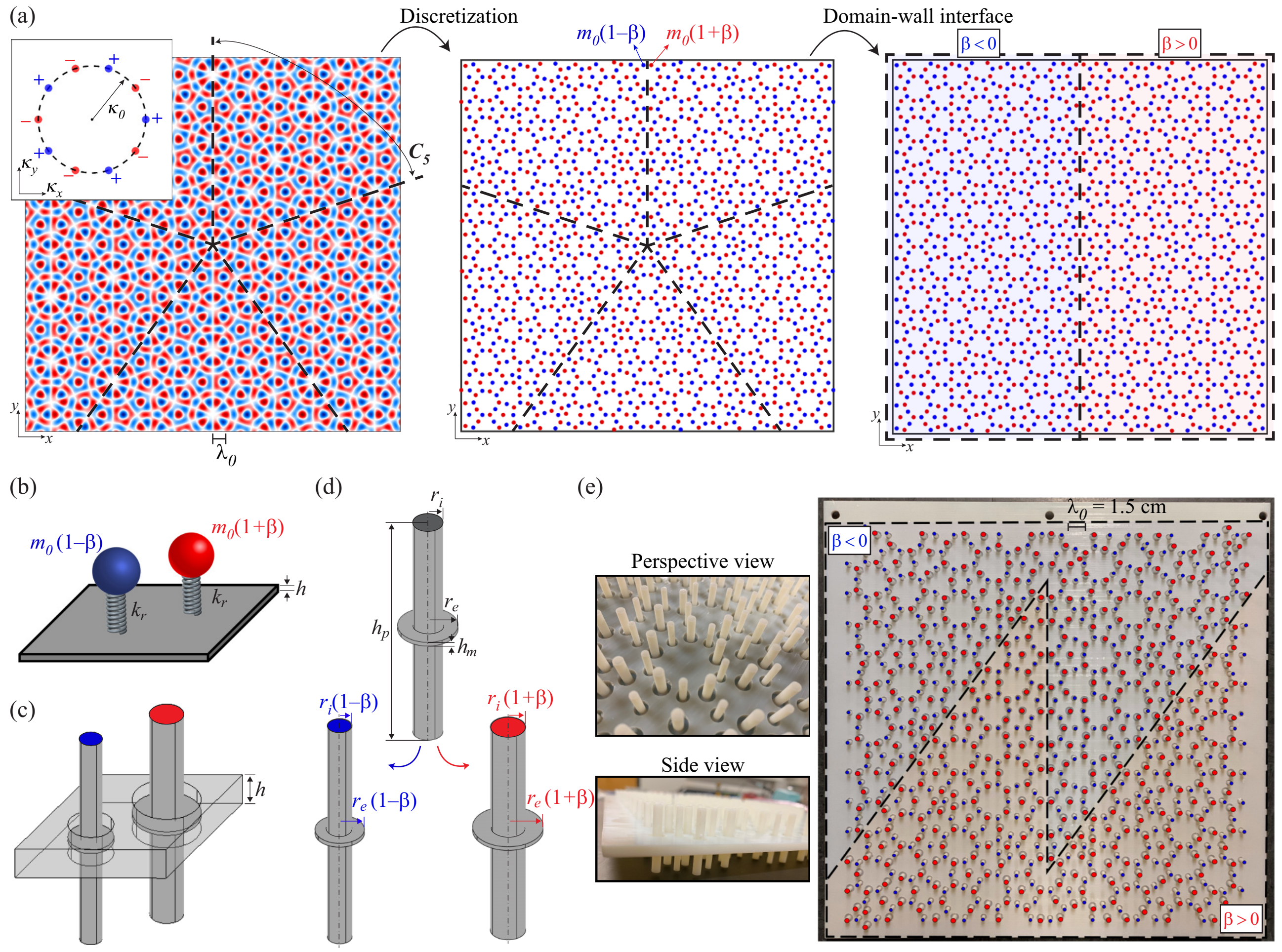

FIG. 1. Design of dimerized quasicrystal (QC) lattices and creation of domain wall interfaces. (a) The quasicrystalline continuous field $\phi(\mathbf{r})$ with C_5 symmetry (left panel). The inset illustrates the Fourier design peaks of alternating signs. The discretization of the field leads to the dimerized C_5 lattice in the middle panel, with red and blue masses parametrized by $m_0(1+\beta)$ and $m_0(1-\beta)$. A straight domain wall interface is formed by contrasting domains with opposite β signs, as shown in the right panel. (b) Implementation of dimerized spring-mass resonators, and (c) analogy to pillar-membrane resonators, whose dimerization illustrated in (d) is achieved via the pillars' radii. (e) Photographs of additive manufactured sample featuring a QC lattice of resonators with a zigzag interface. The locations of bigger and smaller resonators are marked in red and blue circles overlaid on the photograph on the right.

For ease of implementation, the continuous field is discretized to form a point lattice as illustrated in Fig. 1(a). This is done through a level-cut procedure where the peaks and valleys of the continuous field define two sublattices of blue and red points, respectively (for more details, see Appendix A). The color of the points may represent a property such as mass, leading to a convenient dimerization where red and blue masses are respectively parametrized as $m_0(1+\beta)$ and $m_0(1-\beta)$, with m_0 being the baseline mass and β the dimerization parameter. Notice that the positions of the masses alone define a C_{10} quasicrystalline lattice, whose symmetry is maintained when $\beta = 0$ and the masses are equal to m_0. However, when $|\beta| > 0$, a C_5 QC with broken inversion symmetry is formed due to the contrast between blue and red masses. Naturally, β values of opposite signs produce distinct versions of the C_5 QC with opposite inversion symmetry, which are related by interchanging the locations of red and blue masses, or by a rotation of $2\pi/10$.

This parametrization is inspired by similar procedures applied to hexagonal lattices in the context of the VHE, where β is used to break the inversion symmetry of C_6 lattices into C_3 [47,55]. Indeed, the case $N = 6$ in Eq. (1) reproduces the same dimerized honeycomb lattices of such prior works, as illustrated in Appendix A. The dimerization conveniently allows the creation of domain wall interfaces by connecting two regions with β values of opposite signs, as illustrated in Fig. 1(a) for the case of a simple straight interface parallel to the y axis ($N = 10$). In the example of Fig. 1(a), the interface contrasts the red type masses by using negative and positive β parameters respectively at the left and the right domains, while the opposite would produce an interface contrasting blue masses. More complex interfaces composed of multiple lines can be created, as long as each line is defined along one of the axes of rotational symmetry. Figure 1(e) illustrates a zigzag interface similar to those typically employed in the context of the VHE [55], although the higher-order rotational symmetry of the QCs allow for sharper turns. The zigzag interface presented here exhibits two angular turns of 36°, while the periodic C_6 symmetry is restricted to turns of 60°. As we will show, these interfaces support localized modes with waveguiding capabilities that appear to be analogous to those found in C_6 symmetric periodic lattices in the context of the VHE.

In our analysis, the proposed lattices define resonators attached to an elastic plate through springs of constant stiffness k_r, as conceptually illustrated in Fig. 1(b). The dimerization in general leads to two distinct resonators of frequencies $\omega_a = \sqrt{k_r/m_a}$ and $\omega_b = \sqrt{k_r/m_b}$, with masses $m_a = m_0(1-\beta)$ (blue) and $m_b = m_0(1+\beta)$ (red), which are represented in Fig. 1(b) in a typical honeycomb lattice unit cell. This setup is inspired by previous works dealing with elastic analogues to the VHE in elastic plates with honeycomb lattices of resonators [51,55]. When $\beta = 0$, the masses are the same and a Dirac cone is nucleated in the dispersion bands [51], while $|\beta| > 0$ breaks the inversion symmetry of the unit cell and opens up topological band gaps which support interface states [55]. Here we extend this setup to the configurations based on the dimerized quasicrystalline lattices [Fig. 1(a)], with the aim of identifying interface states with similar features. Our practical implementation consists of membrane-pillar resonators composed of a thin circular membrane of thickness h_m and a cylindrical pillar of height h_p, embedded in a baseline plate of thickness h, as depicted in Fig. 1(c). The baseline resonator is characterized by external (membrane) and internal (pillar) radii r_e and r_i, respectively, with the dimerization leading to two distinct resonators as depicted in Fig. 1(d). For example, when $\beta > 0$, the smaller resonator (blue) is characterized by external and internal radii $r_e(1-\beta)$ and $r_i(1-\beta)$, while the bigger resonator (red) by $r_e(1+\beta)$ and $r_i(1+\beta)$. For the experimental part of this work, we test the QC plate shown in Fig. 1(e), which features a zigzag domain wall interface and was fabricated through additive manufacturing (see Sec. IV for more details on the fabrication and geometrical parameters).

III. SPECTRAL PROPERTIES: BAND INVERSION AND INTERFACE STATES

We begin by investigating the spectral properties of the quasicrystalline plates, revealing a band inversion of the bulk bands that is accompanied by the appearance of in-gap bands of interface states. The phenomenon is first numerically illustrated by considering the plate with spring-mass resonators due to the relative low computational cost and reduced wave/vibration analysis complexity. The same strategy is then implemented on the manufactured plate leveraging membrane-pillar resonators, where waveguiding along the zigzag interface is experimentally demonstrated. The flexural motion of the thin homogeneous elastic plate is investigated based on the Kirchhoff theory, with the governing equation in the frequency domain expressed as [51,55]

$$D\nabla^4 \mathrm{w} - \rho h \omega^2 \mathrm{w} = k_r \sum_i (\mathrm{w} - \mathrm{w}_i)\, \delta\, (\mathbf{r} - \mathbf{p}_i)\,, \tag{2a}$$

$$-\, m_i \omega^2 \mathrm{w}_i + k_r\, (\mathrm{w}_i - \mathrm{w}(\mathbf{p}_i)) = 0, \tag{2b}$$

where $\mathrm{w} = \mathrm{w}(x, y)$ is the out-of-plane displacement of the plate, ω is the angular frequency, and the subindex i represents the ith resonator of position $\mathbf{p}_i$ and mass m_i, characterized by a displacement w_i. The plate has thickness h, elastic modulus E, mass density ρ, Poisson ratio ν, and flexural stiffness $D = Eh^3/[12(1-\nu)]$.

Our approach relies on eigenfrequency and eigenmode computations for representative finite domains containing a straight interface, which are illustrated in Figs. 2(a) and 2(d) for the periodic (hexagonal) and quasicrystalline cases, respectively. The dimerized honeycomb lattice is first presented to connect our approach and results to known features of the VHE [55], which afterwards are analogously observed in the QC lattice. The domains are constructed by considering a plate of finite size $L_x = 25\lambda_0$ and $L_y = 60\lambda_0$ along the x and y axes, with simply supported boundary conditions at the edges ($w = 0$). The eigenfrequencies and eigenmode shapes are computed through a discretized form of Eq. (2) solved within the ABAQUS computational environment (see Appendix B for more details). The straight interface is introduced at the center of the domain extending parallel to the y axis, separating two regions of contrasting β values, namely, $\beta = -\gamma$ and $\beta = \gamma$ at the left and right sides, respectively. Two types of interfaces are possible: when $\gamma > 0$, the interface contrasts resonators with the larger masses $m_0(1+\beta)$ (red), as illustrated in Figs. 2(a) and 2(d), while $\gamma < 0$ corresponds to an interface contrasting the smaller masses $m_0(1-\beta)$ (blue). Varying γ therefore allows for a transition between these two configurations, with the transition point $\gamma = 0$ defining a lattice with no interface since all masses are equal to m_0.

The results in Figs. 2(b) and 2(e) show the variation of the eigenfrequencies with γ for the hexagonal and QC lattices, respectively. For ease of comparison with previous studies [51,55], our results are presented in terms of the normalized frequency $\Omega = \omega a^2 \sqrt{\rho h/D}$, where $a = 2\sqrt{3}\lambda_0/3$ is the resulting hexagonal lattice constant when $N = 6$ is used in Eq. (1). We also employ a baseline resonator frequency $\Omega_0 = 4\pi$, which sets $k_r = 16\pi^2 m_0 D/\rho h a^4$, and a mass ratio of 10, that is, $m_0 =$

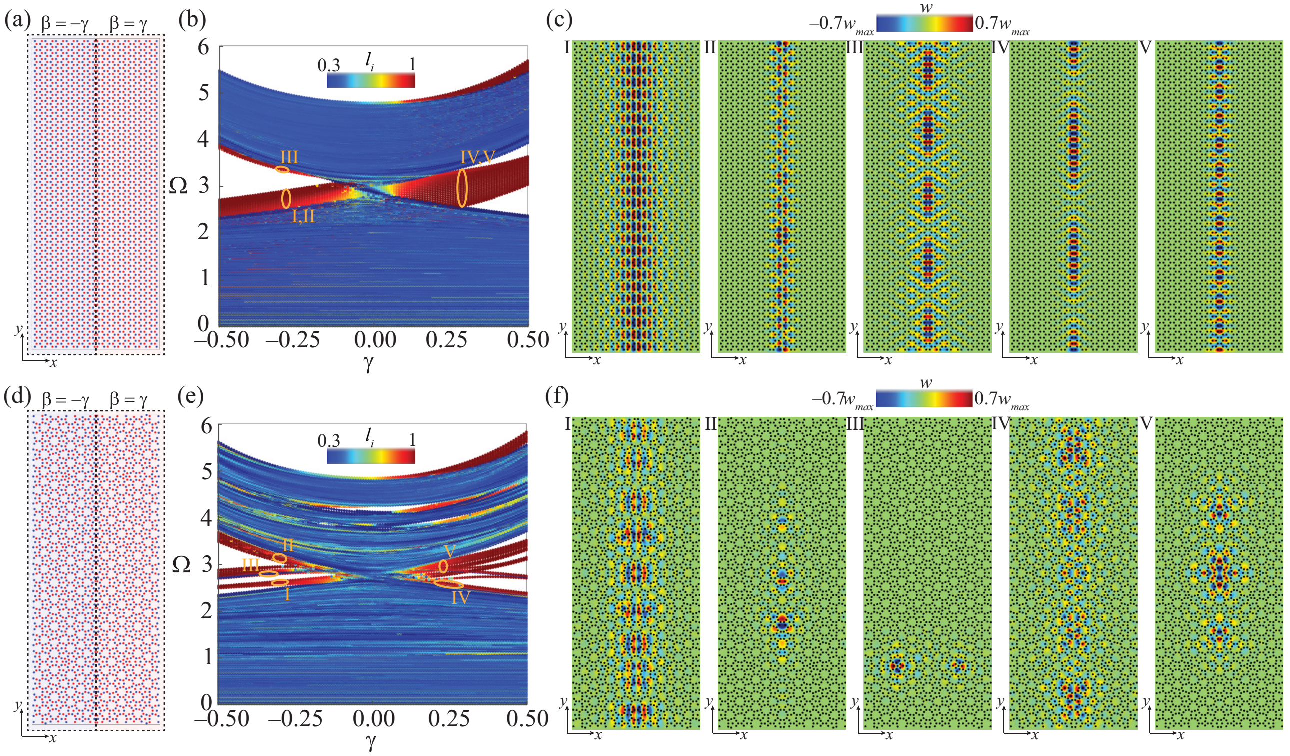

FIG. 2. Identification of interface states for honeycomb (a)–(c) and QC plate (d)–(f). The finite plate featuring a domain wall interface separating regions with opposite dimerization parameter $\beta = \pm\gamma$ (a),(d). The spectrum as a function of γ (b),(e), color-coded by the interface localization factor l_i, showing the band inversion and the appearance of interface states inside the gap. Selected examples from groups of modes marked in (b),(e) are displayed in (c),(f).

$10\rho A_c h$, where $A_c = \sqrt{3}a^2/2$ is the area of the honeycomb lattice unit cell. The eigenfrequencies are color-coded according to an interface localization factor l_i, which is defined as

$$l_i = \frac{\int_{\mathcal{D}_i} \mathrm{w}^2 dA}{\int_{\mathcal{D}} \mathrm{w}^2 dA}, \tag{3}$$

where w is the out-of-plane displacement of the mode shape, $\mathcal{D}$ represents the domain of the plate, and $\mathcal{D}_i$ denotes a smaller domain centered near the region of the interface with 40% of the length L_x, extending uniformly along the y direction. High l_i values indicate eigenfrequencies whose eigenmode shapes are concentrated near the interface (red), while low l_i values correspond mostly to nonlocalized bulk modes (blue). The spectra also typically exhibit modes localized at the edges of the plate, which were filtered out from the plots based on a similar localization factor defined for the edges.

Both the honeycomb and QC plate spectra in Fig. 2 feature a large band gap, defined by the absence of bulk (blue) modes, that undergoes a band inversion as it closes and reopens as a function of γ. This behavior is commonly found in the search for topological states, usually defining phases of different topological properties, and therefore is a strong indicator that topological states will be found when contrasting domains living on opposite sides of the band inversion [50,54]. Without Bloch-based procedures, we are unable to directly observe the inversion of symmetry of band-edge states in momentum space that typically accompanies the band inversion process. However, we can directly observe a series of parallels in the behavior of the finite plate spectra, including the gap closure and reopening, and the existence of interface states. Indeed, due to the presence of the domain wall, we observe that additional bands of modes localized at the interface (red) appear inside the band gaps. These features are reminiscent of those observed in the context of the VHE, and, in the honeycomb lattice, they can be precisely mapped to previously established results. For instance, the gap closing point at around $\Omega = 2.74$ for $\gamma = 0$ in Fig. 2(b) corresponds to the Dirac cone degeneracy identified by the Bloch analysis of the hexagonal unit cell [51]. The degeneracy is lifted for $|\gamma| > 0$ due to the inversion symmetry breaking, opening up a band gap with nontrivial topological properties related to valley Chern numbers of opposite signs at the valley K and K' points [55]. By contrasting two domains with opposite β values, and therefore opposite valley Chern numbers, the existence of interface states is typically identified by considering an x-wise finite strip and imposing periodicity conditions along the y direction. In Fig. 2(b), the bands of interface states contain a finite number of modes that are a result of the finite extent along the y direction, which causes a discretization of the otherwise continuous bands in the finite-strip case. Selected mode shape examples from the groups of bands highlighted in Fig. 2(b) are displayed in Fig. 2(c). In the left half of the spectrum ($\gamma < 0$), there are two groups of modes inside the gap, one at its lower and the other at its upper boundary, containing modes which are antisymmetric (I, II) and symmetric (III) with respect to the interface line, respectively. In the right half ($\gamma > 0$), there is one group of modes inside the gap which are symmetric with respect to the interface (examples IV, V). The correspondence between these results and the analysis typically conducted for periodic lattices based on Bloch-Floquet theory is illustrated through additional numerical results in Appendix B. However, such periodicity conditions cannot be applied in the QC case, which motivates our approach based on the large finite domains.

The QC spectrum in Fig. 2(e) exhibits a similar band inversion with a gap closing point at $\gamma = 0$ around the Dirac cone frequency of the honeycomb lattice. The interface states form a larger number of thinner bands, when compared to the honeycomb lattice, with selected modes displayed in Fig. 2(f) exemplifying their characteristics. A band of antisymmetric modes (I) is present at the lower boundary of the gap for $\gamma < 0$, and migrates to the upper boundary of the gap (V) for $\gamma > 0$. Similarly, a band of symmetric modes migrates from the upper boundary (II) to the lower boundary (IV) of the gap as γ increases and flips sign. While these modes are localized at the interface, in contrast to the hexagonal case they are not necessarily extended throughout the entire interface due to the absence of periodicity (see, for example, modes II and V). The QC also exhibits a thin band of modes inside the gap which are localized in isolated regions away from the interface, as exemplified by mode III. These are reminiscent of intrinsic localized modes found in other investigations of QC lattices [61–64], which are expected to appear even in the absence of defects due to the lack of translational periodicity. More details on the in-gap states of the QC plates are provided through additional mode plots in Appendix B.

Our results illustrate the emergence of interface states due to the broken inversion symmetry of the QC lattice, in analogy to the behavior of hexagonal lattices in the VHE. The finite-elastic-plate analysis provides a prediction of the frequency ranges occupied by the interface states and their features such as symmetric versus antisymmetric mode shapes. These modes can be exploited to create waveguides with sharp turns that leverage the symmetry axes of the resonator lattice. To exemplify, Fig. 3 displays the response of a QC plate with $\gamma = -0.2$ and a zigzag interface for two frequencies that excites the bands (I) and (II) of Fig. 2(e). The harmonic response due to a point source placed at the center of the plate is computed for the selected frequencies through a multiple scattering procedure, which is detailed in previous works [20,51]. We observe that the displacement field is localized at and extends throughout the entire interface, with no evident backscattering at the sharp angular turns. The results are also in agreement with the predicted features of the interface states, with Figs. 3(a) and 3(b) showing respectively antisymmetric and symmetric modes with respect to the interface line, corresponding to the expected behavior of bands (I) and (II) from Fig. 2(e).

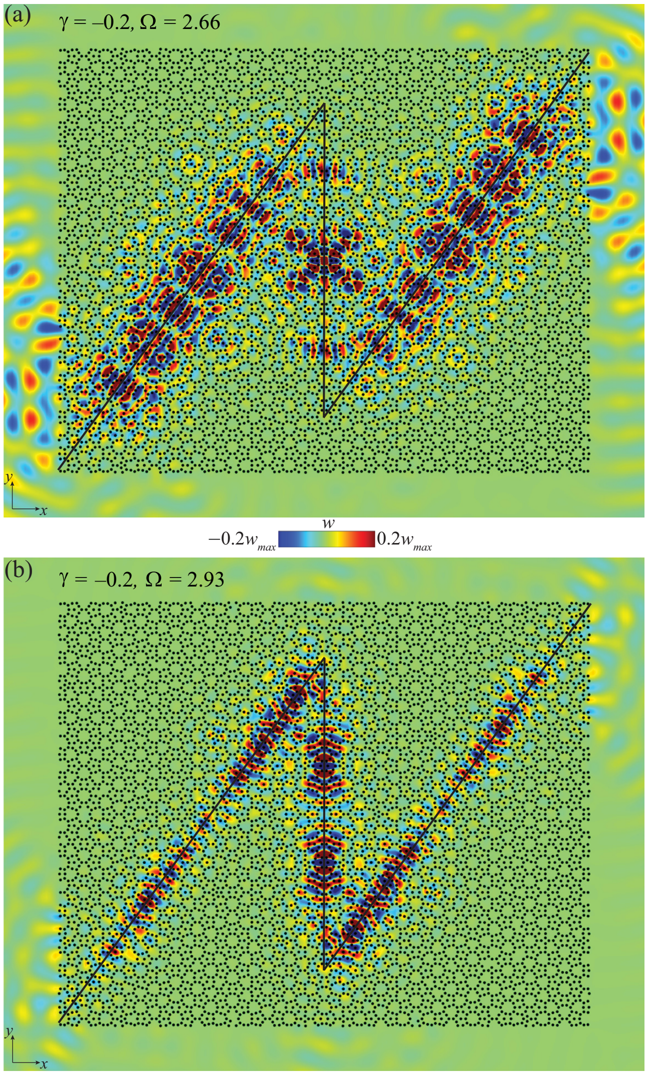

FIG. 3. Harmonic response of QC plate with zigzag interface for selected frequencies, illustrating the excitation of antisymmetric (a) and symmetric (b) interface states that propagate through angular turns of 36°.

IV. EXPERIMENTAL OBSERVATION OF INTERFACE STATES IN QUASICRYSTALLINE ELASTIC PLATE

The physical demonstrator in Fig. 1(e) was fabricated through additive manufacturing due to its geometrical complexity. Specifically, the fabrication was done in a Stratasys PolyJet machine using Vero Rigid material, with the following estimated properties: elastic modulus $E = 3$ GPa, mass density $\rho = 1000$ kg/m^3, and Poisson coefficient $\nu = 0.33$. The zigzag domain wall was chosen to confirm the wave propagation of the interface state in the presence of very sharp angular turns of 36°. The positions of the resonators were obtained from the described design procedures with a fundamental length scale of $\lambda_0 = 1.5$ cm, and the plate has a total size of 39 × 39 cm. The plate is characterized by the following geometrical parameters: $h = 4$ mm, $h_p = 32$ mm, $h_m = 0.5$ mm, $r_e = 3.3$ mm, $r_i = 1.65$ mm, with a dimerization parameter $\beta = 0.15$. These parameters were chosen guided by 3D finite-element simulations to establish the features of the VHE in the periodic (honeycomb) lattice, which are detailed in Appendix C. In particular, when $\beta = 0$ we achieve a Dirac cone degeneracy at the frequency $f = 6915$ Hz, while $\beta = 0.15$ lifts the degeneracy and opens a band gap that extends from $f = 5822$ Hz to $f = 7548$ Hz. Our simulations then confirm the existence of interface states in the QC plate with the zigzag interface at the same frequency range, including a frequency response and a time transient analysis that are also shown in Appendix C, while here we focus on experimental results.

In experimental tests, the out-of-plane motion of the plate (i.e., along the z-axis) is measured by a scanning laser Doppler vibrometer (SLDV). An excitation is provided through a piezoelectric disk placed at the center of the plate (STEMINC model SMD05T04R411). The excitation signal is generated by a computer and amplified by a linear amplifier (PIEZO SYSTEMS EPA-104) before reaching the piezo disk. The motion is recorded across a square grid containing 90 × 90 points, and the results are combined and processed within the MATLAB environment. First, a broad-band sinusoidal chirp signal in the frequency range of 4–16 kHz is used to characterize the frequency response of the plate, which is estimated by taking the ratio between the Fourier transforms of the measured velocity and the input voltage. Figure 4(a) displays the response at two points, one at the interface (I), and the other close to the corner of the plate (II). A large band gap extending approximately from 6 kHz to 13 kHz is observed to appear, due to the broken inversion symmetry from the dimerization with $\beta = 0.15$. While the response near the corner (II) shows an almost uniform gap, the response at the interface (I) highlights an additional resonance peak residing within the gap at 6950 Hz. The response for the entire plate is displayed for two selected frequencies in Fig. 4(b): at $f_1 = 6125$ Hz a typical spatial attenuation occurring inside the gap is shown, while for the resonance peak at $f_2 = 6950$ Hz the response is clearly localized along the zigzag interface. The excited interface state exhibits a symmetric shape similar to those of type V in Fig. 2(f). We also note that there is a significant, albeit uniform, amplitude decay away

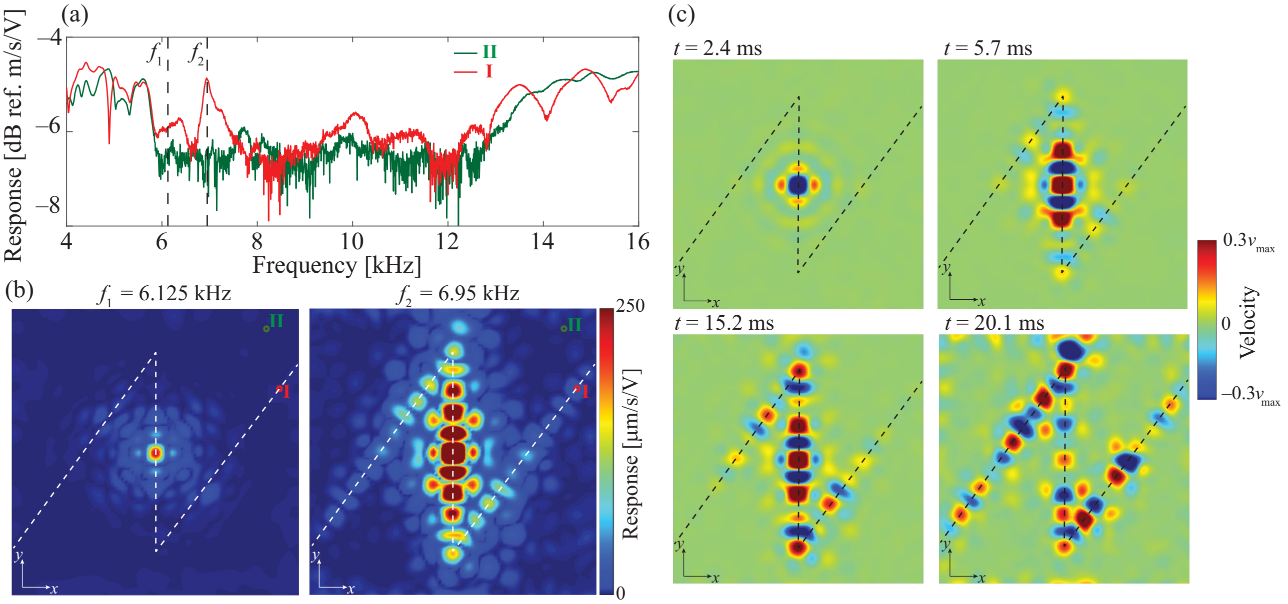

FIG. 4. Experimental observation of interface states in a QC additive manufactured plate. The frequency response of the plate for points I and II (a), which are marked in the response fields for selected frequencies f_1 and f_2 displayed in (b). The resonance peak inside the gap identified at f_2 is characterized by a response concentrated along the zigzag interface. The snapshots for subsequent time instants in (c) illustrate the transient wave propagation along the interface caused by a wave packet centered at f_2.

from the center of the interface. We attribute this behavior to the high dissipation inherently present in the 3D printed material. This statement is also supported by additional numerical simulations presented in Appendix C, where a comparison between the simulated responses with and without dissipation is shown.

After the experimental characterization of the frequency spectra and identification of the interface state frequency, an additional transient test is performed to illustrate the temporal wave propagation along the zigzag interface of the QC plate. A sinusoidal wave packet centered at the frequency $f = 6950$ Hz with 100 cycles is sent to the piezoelectric patch, with the response simultaneously recorded by the SLDV. The panels in Fig. 4(c) show subsequent snapshots of the recorded wave field, with a video animation of the entire response included in the Supplemental Material [65]. Due to the high dissipation of the material, the color axis is separately scaled for each snapshot in a range corresponding to 30% of the recorded maximum velocity $v_{\max}$ at that time instant. The results clearly show the waves propagating along the interface with no evident backscattering, and successfully passing through the angular corners of 36°, thus confirming the expected features from the interface states in the QC plate induced by the broken inversion symmetry.

V. CONCLUSIONS

This paper proposes a framework that extends the mechanism of inversion symmetry breaking and its utilization for the creation of domain wall interfaces to QC lattices. Inspired by the features of the VHE in periodic lattices, our results confirm the existence of a band inversion accompanied by the appearance of interface states upon varying a dimerization parameter. Both numerical and experimental results illustrate possibilities for waveguiding along interfaces with sharper turns enabled by the higher-order rotational symmetries of QCs, thus extending the behavior previously restricted to symmetry orders of periodic lattices. While these features are illustrated for elastic waves, they can be more generally applied to other types of waves including acoustic, electromagnetic, and even to quantum systems. Indeed, our results pave the way for the exploration of topological states in QCs through a simple inversion-symmetry-breaking procedure, which does not require magnetic fields or active components to break time-reversal symmetry. While a simple dimerization was used here, other strategies to break inversion symmetry or other types of symmetries in QCs may be explored in future studies. For example, breaking out-of-plane mirror symmetry may enable the observation of spin-orbit coupling towards an implementation of the SHE [42,45] in passive QCs.

Although our results demonstrate a strong correlation to the VHE both through numerical and experimental results, future efforts should be directed towards a rigorous understanding of the underlying topological properties and features that are challenging to explore in the absence of Bloch-Floquet periodicity analyses. These may include the observation of momentum space features such as the Dirac cone, the localization of the Berry curvature, and computation of topological invariants such as the valley Chern number, or any equivalent features that may be present in the QC lattices. Other strategies to characterize the topology of aperiodic systems such as using the Bott index may be explored [39]. On the practical side, our results show strong evidence of backscattering-free wave propagation, but a more rigorous analysis and quantification of backscattering alongside comparisons with trivial or defect-based waveguides is an important task for future studies [66–68]. In addition, understanding the momentum space features mentioned above may lead better efficiency in the excitation of these states through wave-vector matching [50].

ACKNOWLEDGMENTS

D. Beli and M. I. N. Rosa contributed equally to this work. D. Beli and C. De Marqui Jr. gratefully acknowledge the support from the São Paulo Research Foundation (FAPESP) through Grant Reference Nos. 2018/18774-6, 2019/22464-5, and 2018/15894-0 (Research project—Periodic structure design and optimization for enhanced vibroacoustic performance: ENVIBRO). M. I. N. Rosa and M. Ruzzene gratefully acknowledge the support from the National Science Foundation (NSF) through Grant EFRI 1741685 and from the Army Research Office through Grant W911NF-18-1-0036.

APPENDIX A: DESIGN OF DIMERIZED QUASICRYSTAL LATTICES

This section provides a more detailed explanation of the steps involved in the design strategy to obtain dimerized quasicrystal (QC) lattices. Consider again Eq. (1), which expresses the two-dimensional (2D) quasiperiodic continuous distribution by using a plane-wave superposition. In this representation, each Fourier peak in 2D reciprocal space corresponds to a plane wave, either a sine or cosine function, and its angle in 2D reciprocal space corresponds to the wave direction in the 2D physical space. To facilitate comprehension, Fig. 5 illustrates this plane-wave superposition process, which generates a continuous field for distributions with 3/6-, 5/10-, and 7/14-fold symmetries. This illustration is performed within a small domain centered at the physical origin ($x = 0$ and $y = 0$) for visualization purposes. It is important to note that the rotational symmetric location of the Fourier peaks, together with the proposed phase term, $\phi = n\pi + \pi/2$ in Eq. (1), produces periodic/quasiperiodic continuous fields in physical space with complementary mirror symmetry areas in the lines related to the chosen rotational fold symmetry.

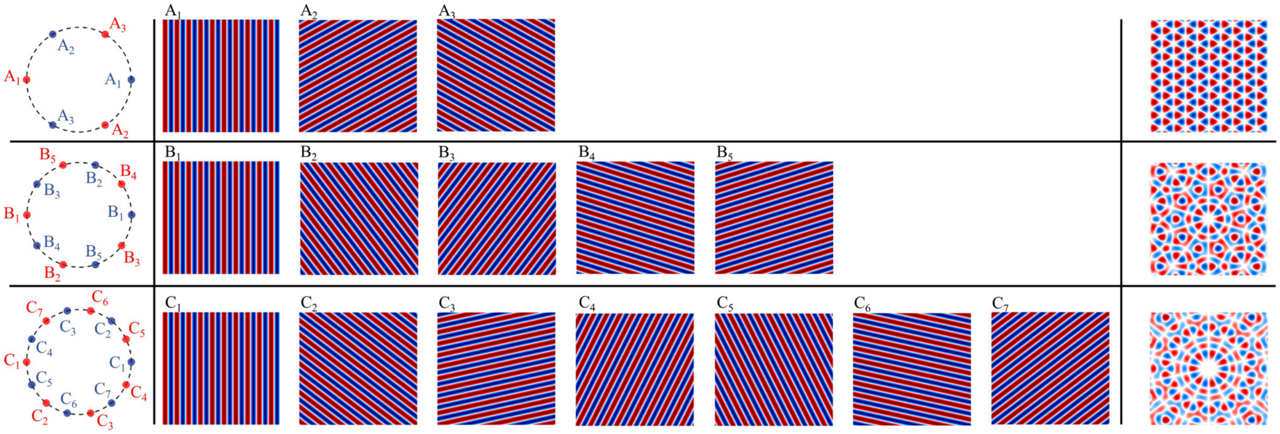

FIG. 5. Detailed plane-wave superposition strategy in reciprocal space for the design of 2D continuous quasiperiodic fields with dimerized areas for 3/6- (top row), 5/10- (middle row), and 7/14-fold symmetries (bottom row). The complex Fourier peaks with alternating phase are represented by blue and red circles in reciprocal space (left column), single-wave representation for each corresponding Fourier peak in physical space (middle column), and the resulting 2D continuous field in physical space (right column).

The resulting continuous field in physical space is a 3D surface as illustrated in Fig. 6 using the 10-fold quasiperiodic distribution obtained in Fig. 5 as an example. The next step involves discretizing this continuous field through a level-cut procedure. Initially, a specific level cut $|\xi|$, ranging between 0 and 1, is defined, where 0 means cutting the surface at its center, $+1$ means touching the surface at its highest peaks, and -1 means touching the surface at its lowest peaks. Consequently, a plane intersects the surface along the positive z axis at the defined level $+\xi$. The local peaks are identified by the intersection contours of the 3D surface and the defined plane, with each contour center defining a lattice site. As displayed in Fig. 6, this process yields the sublattice `A` with fivefold symmetry composed exclusively of sites `A`. Similarly, the same procedure is applied to obtain the complementary fivefold sublattice `B`, in this case a plane intersects the surface along the negative z axis at the defined level $-\xi$. Finally, the resulting dimerized lattice emerges through the superimposition of both sublattices `A` and `B`. The choice of the level-cut parameter influences the number of sites for each sublattice of the QCs, and a representative value of $\xi = 0.44$ was used in this work for the 5/10-fold symmetry.

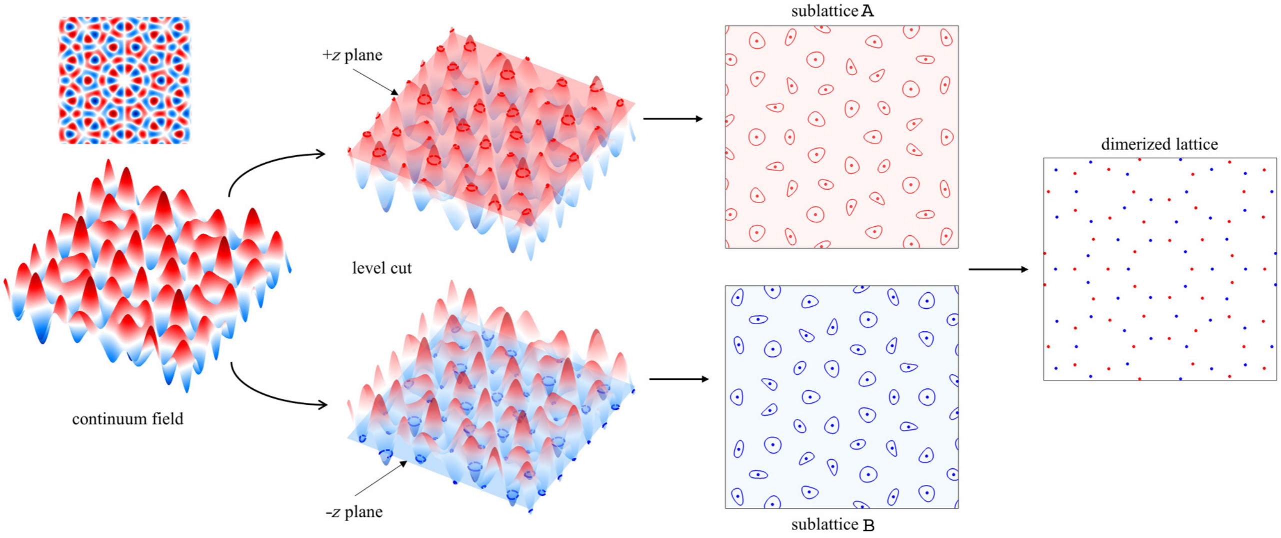

FIG. 6. Level-cut procedure to transform the continuous field in a QC dimerized lattice: continuous field in 2D (from Fig. 5) and 3D views (left column), level-cut procedure using positive ($+\xi$) and negative ($-\xi$) planes to generate, respectively, rotational symmetric sublattices `A` and `B` (middle columns). The resulting dimerized lattice is composed of the superimposition of sublattices `A` and `B` (right column).

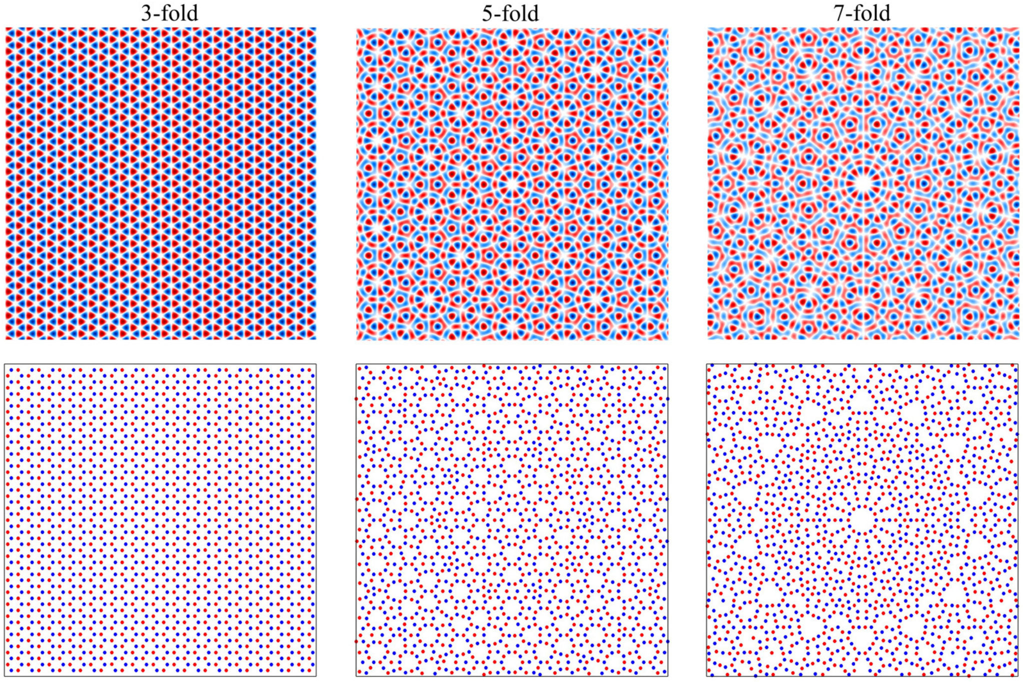

FIG. 7. Quasiperiodic continuous distributions (top row) and dimerized lattice (bottom row) based on the proposed design strategy for 3/6- (left column), 5/10- (middle column), and 7/14-fold (right column) symmetry.

The same wave superposition and level-cut procedures can be applied to obtain dimerized lattices with other rotational fold symmetries as presented in Fig. 7 for large domains, where 3/6-fold symmetry is obtained with $\xi = 0.50$ and 7/14-fold symmetry is obtained with $\xi = 0.31$. The honeycomb lattice can be obtained by the proposed design strategy as a particular case when $N = 6$ is used in Eq. (1). This is particularly interesting due to the relevance of the (dimerized) honeycomb lattice in several topological phenomena as explained in the main text and further detailed in the following appendices.

APPENDIX B: SPECTRAL PROPERTIES: BAND INVERSION AND INTERFACE STATES

This appendix provides additional details regarding the numerical simulations conducted using a 2D elastic plate with lumped mass-spring resonators positioned at the sites of the dimerized lattices provided by the presented design strategy. Furthermore, supplementary results concerning the spectral properties of both 3/6-fold and 5/10-fold lattices are presented to support the assertions made in the main text.

1. Finite-element numerical simulations in ABAQUS

To obtain the results of Fig. 2 in the main text, modal analysis is performed using the Lanczos solver implemented in the ABAQUS software package. The plates are of size $L_x = 50a$ and $L_y = 120a$, with thickness $h = 0.01a$, and simply supported boundary conditions are considered at the edges. Standard 2D structural elements with three nodes based on the Kirchhoff theory are used to discretize the elastic plates. The plate behavior is modeled using a homogeneous linear elastic constitutive law with $\rho = 2700$ kg/m^3, $E = 70$ GPa, and $\nu = 0.33$. The resonators are modeled by attaching spring-mass systems to the plates. Specifically, springs with $k_r = 1.6 \cdot 10^3$ kN/m acting along the out-of-plane direction are used to connect the point mass elements with $m_0 = 1.3 \cdot 10^3$ kg to the plates. The band inversion results through modal analysis are computed by uniformly discretizing the parameter β using 121 values in the range $[-0.5, 0.5]$.

2. Dispersion results for the sixfold lattice

The dispersion results for the honeycomb lattice, characterized by 3/6-fold symmetry, are obtained through Bloch-Floquet periodic conditions and are compared with the spectral results obtained through modal analysis. Its band structure is depicted in Fig. 8(a). When considering equal resonators in both sublattices `A` and `B` (i.e., $\beta = 0$), a Dirac point emerges at the reciprocal point K, positioned at the intersection between the first and second bulk bands around $\Omega = 2.73$. When the lattice has dimerized resonators (i.e., $\beta = \pm 0.3$) a band gap opens around the Dirac point, and the bulk branches remain the same for $\beta = +0.3$ and $\beta = -0.3$. This observation serves as significant evidence for a topological transition in mirror-symmetric honeycomb cells with the valley Hall effect (VHE), which

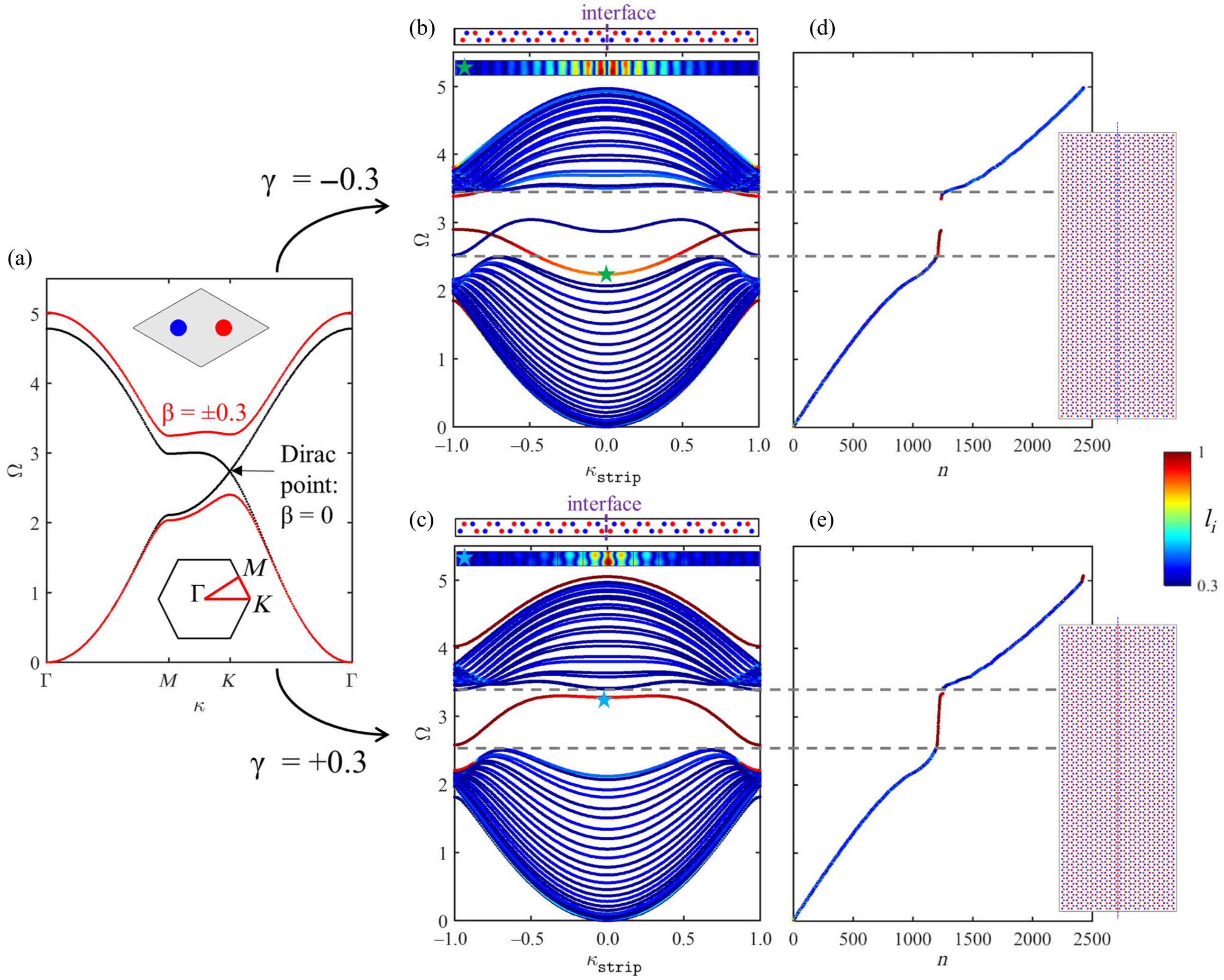

FIG. 8. Dispersion and spectral results of the 2D hexagonal plate: band structure for $\beta = 0$ and $\beta = \pm 0.3$ (dimerization) (a), finite-strip dispersion for $\gamma = -0.3$ (b) and $\gamma = +0.3$ (c), and natural frequencies (obtained by modal analysis) of the complete plate for $\gamma = -0.3$ (d) and $\gamma = +0.3$ (e). The colors in (b)–(e) represent the localization factor described Eq. (3). The dashed line represents the band-gap region that matches in the finite strip and in the complete plate, and the localized modes at the interface match in both cases.

was confirmed by the computation of Chern topological invariants in several works [42,45,55,69,70]. As extensively investigated in literature, the Chern number exhibits opposite values in honeycomb domains with mirror symmetry breaking. Consequently, when these domains with $\beta = +0.3$ and $\beta = -0.3$ are juxtaposed, an interface with contrasting red (i.e., heavy) or blue (i.e., light) masses is created, which supports the propagation of topological modes.

To further illustrate the connection of our results with the VHE, we consider a honeycomb armchair finite strip along x-direction constructed with mirror-symmetry-breaking domains. While the left domain of the strip presents 12 unit cells with a certain dimerization parameter β, its right domain also with 12 unit cells presents an opposite dimerization parameter $-\beta$. Therefore, at the middle of the strip an interface is created with two contrasting masses, where $\gamma < 0$ for light masses and $\gamma > 0$ for heavy masses. In order to compute the finite-strip dispersion, the left and right boundaries (i.e., along x) are free, and Bloch-Floquet periodic conditions are applied on the top and bottom boundaries (i.e., along y) with a normalized wave number $k_{\texttt{strip}} = k_{y\text{S}}.a_{\text{S}}/\pi$, where $k_{y\text{S}}$ and a_{S} are, respectively, the wave number and the strip length along the y direction. The configuration of the finite strips and their dispersion analysis are presented in Figs. 8(b) and 8(c) for $\beta = -0.3$ and $\beta = +0.3$. The localization parameter defined in Eq. (3) is used to distinguish the modes localized at the interface. In both cases, the topological wave branch appears within the band gap and the corresponding topological wave mode exhibits higher amplitude around the interface. Previous studies have demonstrated that for

$\beta < 0$, the topological wave branch nearly touches the bulk bands at the lower limit of the gap, while for $\beta > 0$, it almost touches the bulk bands at the upper limit of the gap [45,55].

The spectral results (i.e., modal analysis) for the complete finite plate with the same interface are shown in Figs. 8(d)–8(e) for $\beta = -0.3$ and $\beta = +0.3$, respectively. The comparison between the finite-strip dispersion (infinite along y) and the modes of the finite (along both x and y) plate shows good agreement in terms of both band-gap locations and frequencies of the interface states. More importantly, the results show that the localized interface states of the finite plate define a dense sampling of the topological valley interface state identified in the finite-strip dispersion. Thus, despite the loss of information concerning the group velocity and wave-mode shape of the interface states, we can establish an equivalence between the Bloch-Floquet results on the finite strip and the modal approach for the finite plate. The modal analysis serves as a reliable approximation to infer the band gaps and interface state behavior in QC lattices, where the lack of translational periodicity prevents the application of Bloch-Floquet periodic conditions.

3. Extra spectral results for the 10-fold lattice

The band inversion results shown in Fig. 2 for the 10-fold QC lattice are further illustrated in Fig. 9, providing more detailed information for $\beta = -0.3$ and $\beta = +0.3$. This additional analysis allows for better differentiation of the various modes that emerge within the band gap. By representing the modes as a function of the solution number, it becomes possible to observe their evolution and grouping. It is important to note that the dimerization parameter remains the same as in the sixfold results, resulting in band gaps with similar frequency range. However, several group of modes appear within the band gap and only few of these groups are concentrated along the complete interface and related to the inversion symmetry breaking, more specifically the groups `A` and `F` for $\beta = -0.3$ and `A` and `D` for $\beta = +0.3$. In contrast to the honeycomb lattice, both types of interfaces (contrasting heavy or light masses) feature modes which can be both symmetric and antisymmetric with respect to the interface. The antisymmetric modes predominantly occupy the lower boundary of the band gap, while the symmetric modes are distributed across the middle and upper boundaries. In addition, there is another group of modes localized around specific points or regions resembling defect states. These localized modes may arise due to the translational periodicity breaking intrinsic in the QCs [63,71].

APPENDIX C: FINITE-ELEMENT NUMERICAL SIMULATION OF INTERFACE STATES IN THE 3D ELASTIC PLATES

This section presents 3D finite-element (FE) numerical results for the dispersion analysis of the honeycomb unit cell (i.e., sixfold symmetry) as well as frequency and time response simulations of the 10-fold elastic plate depicted in Fig. 1, whose the experimental results are presented in Fig. 4.

1. Dispersion results for the sixfold elastic plate

The design of the experimental plate prototype was guided by 3D FE simulations first conducted on the

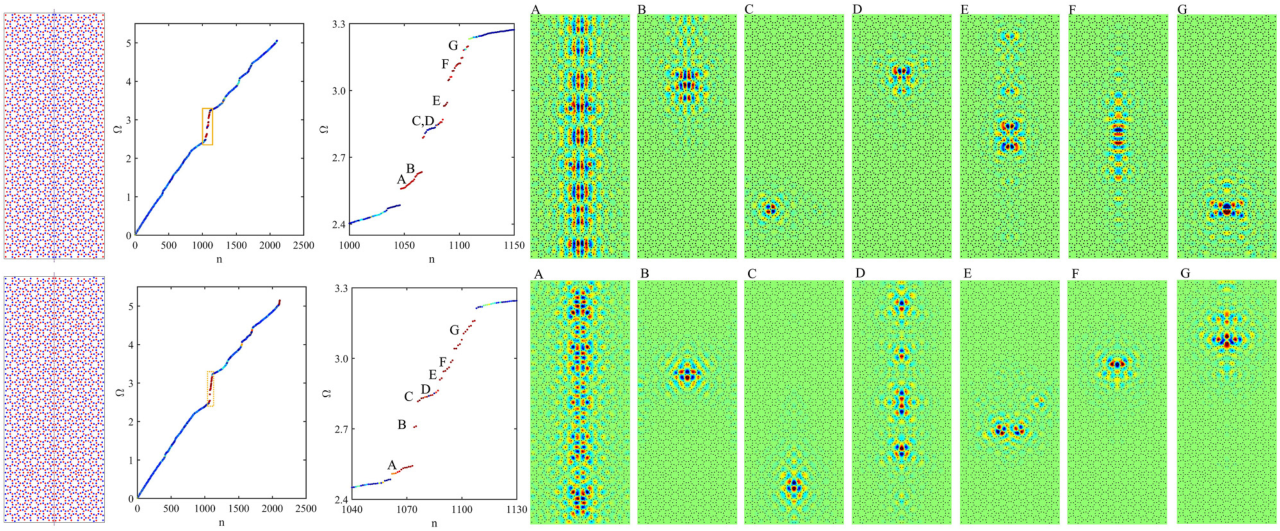

FIG. 9. Extra spectral results for the 2D 10-fold lattice for $\beta = -0.3$ (top row) and $\beta = +0.3$ (bottom row): dimerized lattice distribution (a), natural frequencies of the complete plate (b), zoom at the frequency zone with localized modes at the interface (c), and the group of modes for each frequency zone (d). The most important localized modes are the ones that highlight the entire interface such as group `A` for $\pm\beta$, but some localization around specific areas also appears such as group `B` for $\pm\beta$.

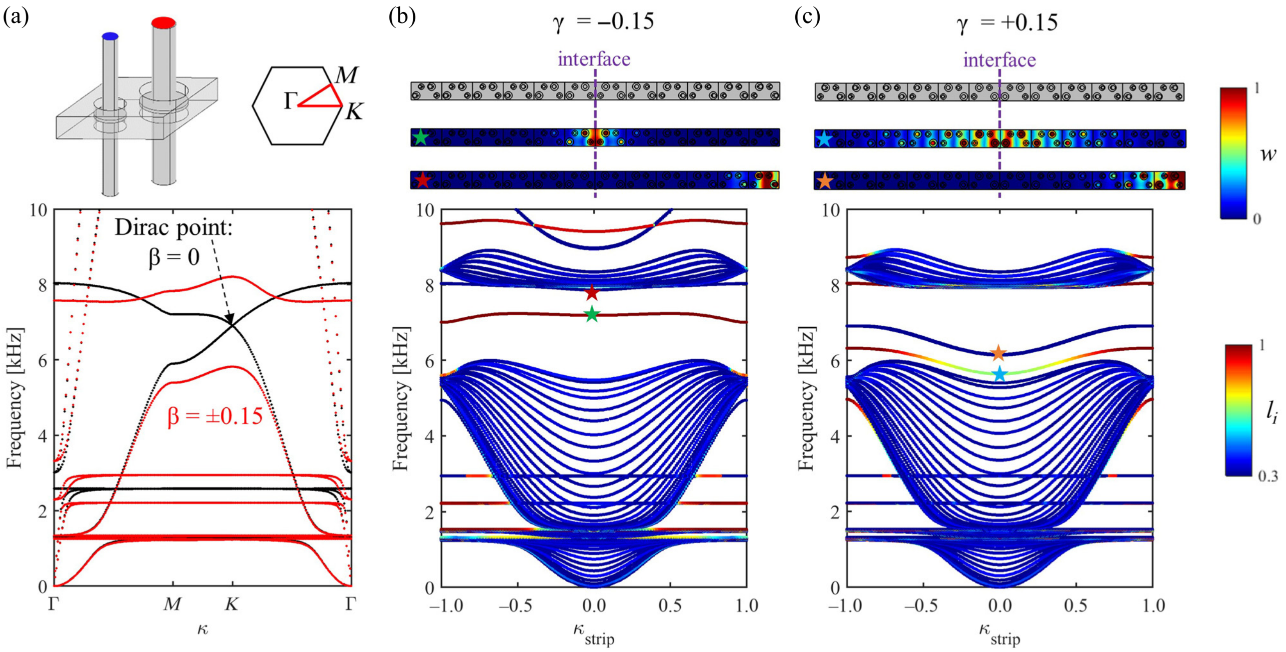

FIG. 10. Dispersion results of the 3D hexagonal plate: band structure with $\beta = 0$ (black) and $\beta = \pm 0.15$ (red) using a single unit cell (a), analysis of the dispersion strip for $\gamma = -0.15$ (b), and analysis of the dispersion strip for $\gamma = +0.15$ (c). It is possible to observe the topological states inside the band gaps (from about 6 kHz to 8 kHz) for both cases, which are characterized by high localization index (in red). The interface and edge modes are depicted for both cases at $\kappa_{\texttt{strip}} = 0$.

honeycomb lattice to identify the presence of the quantum valley Hall effect. In Fig. 10 the band structure for the 3D honeycomb unit cell with membrane-pillar resonators confirms the nucleation of a Dirac point when $\beta = 0$. This degeneracy in the dispersion can be seen as a topological transition in honeycomb configurations supporting valley

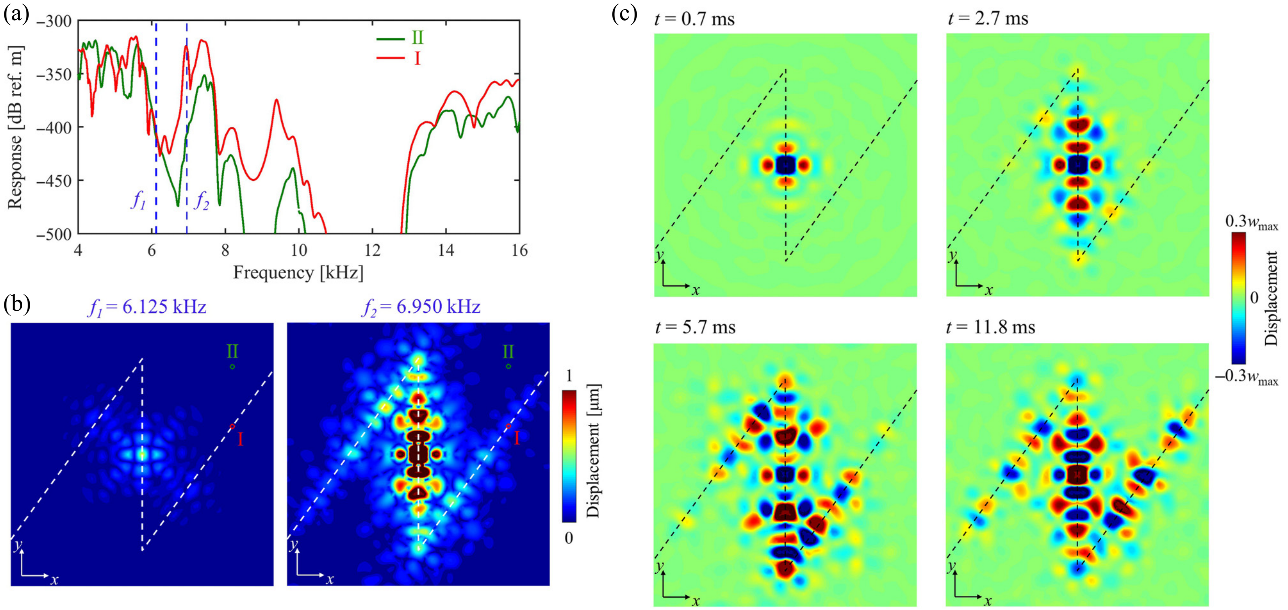

FIG. 11. Finite-element simulation of the 3D elastic plate with interface states in the 10-fold symmetry. Harmonic frequency response at the interface (I) and at the bulk (II) regions (a), the corresponding out-of-plane displacement field at an attenuation zone, and at an interface mode frequency (b). Different snapshots of time response for a burst sine signal excitation at the interface with center frequency of 6.95 kHz (c).

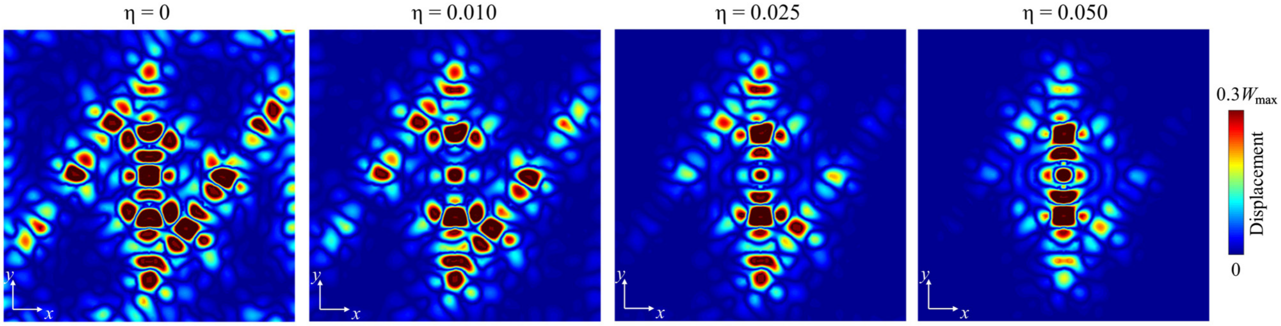

FIG. 12. Influence of the proportional damping in the displacement field of the interface state for harmonic excitation in the middle of the 10-fold elastic plate. Increasing the damping leads to localization closer to the excitation, and hence, the entire interface is not highlighted. A good match between experimental and numerical results occurs for $\eta \approx 0.02$, which is used in the numerical simulations of Fig. 11.

Hall states. When a dimerization $\beta = \pm 0.15$ is induced in the properties of the membrane-pillar resonators, a band gap opens around the Dirac point. In addition, the analysis of the dispersion strip, composed of two domains with inversion symmetric breaking and with six unit cells each, confirms that the topological interface modes with a nonzero group velocity lie inside the band gap. Because of higher slope and touching in the lower gap boundary, the case with $\gamma = +0.15$ (big resonators at the interface) is chosen to create the interface in the 10-fold QC configuration. The wave-mode shapes of the honeycomb strip present a localization only at the interface similar to the case in Appendix B.

2. Frequency and time results for the 10-fold elastic plate

After confirming the existence of topological valley states in the 3D honeycomb configuration, the 3D QC plate presented in Fig. 1 is investigated and its numerical results are shown in Fig. 11. The frequency forced response results show a clear interface state around 7 kHz when a point at the interface is analyzed, while only vibration attenuation is observed for a point at the bulk domain. A proportional damping of $\eta = 0.02$ has been used, which causes a vibration attenuation along the interface when the vibration travels away from the excitation. The FE numerical simulation captures a similar dynamic behavior observed in the experiments, which can be used to explain the attenuation along the interface. Additional frequency-domain simulations with different levels of structural damping for the interface sate frequency are depicted in Fig. 12, confirming that the interface mode localizes along the entire interface without backscattering for lower dissipation levels.

The time-response simulations for the damping $\eta = 0.02$, also depicted in Fig. 11, show good agreement with the experimental results and confirm that the wave packet propagates along the complete interface, even with corners, with the amplitude attenuation related to the structural damping. Therefore, the interface created in the QC plate with broken inversion symmetry is similar to a topological waveguide, enabling higher flexibility in creating 1D circuits with sharp turns in 2D domains when compared to the honeycomb counterpart due to the higher-order rotational symmetry.

[1] M. Zahid Hasan and Charles L. Kane, Colloquium: topological insulators, Rev. Mod. Phys. **82**, 3045 (2010).

[2] Alexander B. Khanikaev, S. Hossein Mousavi, Wang-Kong Tse, Mehdi Kargarian, Allan H. MacDonald, and Gennady Shvets, Photonic topological insulators, Nat. Mater. **12**, 233 (2013).

[3] Ling Lu, John D. Joannopoulos, and Marin Soljačić, Topological photonics, Nat. Photonics **8**, 821 (2014).

[4] Zhaoju Yang, Fei Gao, Xihang Shi, Xiao Lin, Zhen Gao, Yidong Chong, and Baile Zhang, Topological acoustics, Phys. Rev. Lett. **114**, 114301 (2015).

[5] Guancong Ma, Meng Xiao, and Che Ting Chan, Topological phases in acoustic and mechanical systems, Nat. Rev. Phys. **1**, 281 (2019).

[6] Sebastian D. Huber, Topological mechanics, Nat. Phys. **12**, 621 (2016).

[7] M. Miniaci and R. K. Pal, Design of topological elastic waveguides, J. Appl. Phys. **130**, 141101 (2021).

[8] K. v. Klitzing, Gerhard Dorda, and Michael Pepper, New method for high-accuracy determination of the fine-structure constant based on quantized Hall resistance, Phys. Rev. Lett. **45**, 494 (1980).

[9] David J. Thouless, Mahito Kohmoto, M. Peter Nightingale, and Md den Nijs, Quantized hall conductance in a two-dimensional periodic potential, Phys. Rev. Lett. **49**, 405 (1982).

[10] Noah P. Mitchell, Lisa M. Nash, Daniel Hexner, Ari M. Turner, and William T. M. Irvine, Amorphous topological insulators constructed from random point sets, Nat. Phys. **14**, 380 (2018).

[11] Emil Prodan, Virtual topological insulators with real quantized physics, Phys. Rev. B **91**, 245104 (2015).

[12] Yaacov E. Kraus and Oded Zilberberg, Quasiperiodicity and topology transcend dimensions, Nat. Phys. **12**, 624 (2016).

[13] Yaacov E. Kraus, Yoav Lahini, Zohar Ringel, Mor Verbin, and Oded Zilberberg, Topological states and adiabatic pumping in quasicrystals, Phys. Rev. Lett. **109**, 106402 (2012).

[14] Yaacov E. Kraus and Oded Zilberberg, Topological equivalence between the Fibonacci quasicrystal and the Harper model, Phys. Rev. Lett. **109**, 116404 (2012).

[15] David J. Apigo, Kai Qian, Camelia Prodan, and Emil Prodan, Topological edge modes by smart patterning, Phys. Rev. Mater. **2**, 124203 (2018).

[16] David J. Apigo, Wenting Cheng, Kyle F. Dobiszewski, Emil Prodan, and Camelia Prodan, Observation of topological edge modes in a quasiperiodic acoustic waveguide, Phys. Rev. Lett. **122**, 095501 (2019).

[17] Xiang Ni, Kai Chen, Matthew Weiner, David J. Apigo, Camelia Prodan, Andrea Alù, Emil Prodan, and Alexander B. Khanikaev, Observation of hofstadter butterfly and topological edge states in reconfigurable quasi-periodic acoustic crystals, Commun. Phys. **2**, 55 (2019).

[18] Raj Kumar Pal, Matheus I. N. Rosa, and Massimo Ruzzene, Topological bands and localized vibration modes in quasiperiodic beams, New J. Phys. **21**, 093017 (2019).

[19] Yiwei Xia, Alper Erturk, and Massimo Ruzzene, Topological edge states in quasiperiodic locally resonant metastructures, Phys. Rev. Appl. **13**, 014023 (2020).

[20] Marc Martí-Sabaté and Dani Torrent, Edge modes for flexural waves in quasi-periodic linear arrays of scatterers, APL Mater. **9**, 081107 (2021).

[21] Matheus I. N. Rosa, Yuning Guo, and Massimo Ruzzene, Exploring topology of 1D quasiperiodic metastructures through modulated Lego resonators, Appl. Phys. Lett. **118**, 131901 (2021).

[22] Yaacov E. Kraus, Zohar Ringel, and Oded Zilberberg, Four-dimensional quantum Hall effect in a two-dimensional quasicrystal, Phys. Rev. Lett. **111**, 226401 (2013).

[23] Matheus I. N. Rosa, Massimo Ruzzene, and Emil Prodan, Topological gaps by twisting, Commun. Phys. **4**, 130 (2021).

[24] Mikito Koshino and Hiroki Oka, Topological invariants in two-dimensional quasicrystals, Phys. Rev. Res. **4**, 013028 (2022).

[25] D. Shechtman, I. Blech, D. Gratias, and J. W. Cahn, Metallic phase with long-range orientational order and no translational symmetry, Phys. Rev. Lett. **53**, 1951 (1984).

[26] Dov Levine and Paul Joseph Steinhardt, Quasicrystals: A new class of ordered structures, Phys. Rev. Lett. **53**, 2477 (1984).

[27] Steurer Walter and Sofia Deloudi, *Crystallography of Quasicrystals: Concepts, Methods and Structures* (Springer Science & Business Media, New York, 2009), Vol. 126.

[28] Dominic V. Else, Sheng-Jie Huang, Abhinav Prem, and Andrey Gromov, Quantum many-body topology of quasicrystals, Phys. Rev. X **11**, 041051 (2021).

[29] Jiahao Fan and Huaqing Huang, Topological states in quasicrystals, Front. Phys. **17**, 13203 (2022).

[30] Duc-Thanh Tran, Alexandre Dauphin, Nathan Goldman, and Pierre Gaspard, Topological Hofstadter insulators in a two-dimensional quasicrystal, Phys. Rev. B **91**, 085125 (2015).

[31] Jean-Noël Fuchs and Julien Vidal, Hofstadter butterfly of a quasicrystal, Phys. Rev. B **94**, 205437 (2016).

[32] Callum W. Duncan, Sourav Manna, and Anne E. B. Nielsen, Topological models in rotationally symmetric quasicrystals, Phys. Rev. B **101**, 115413 (2020).

[33] Miguel A. Bandres, Mikael C. Rechtsman, and Mordechai Segev, Topological photonic quasicrystals: Fractal topological spectrum and protected transport, Phys. Rev. X **6**, 011016 (2016).

[34] Dániel Varjas, Alexander Lau, Kim Pöyhönen, Anton R. Akhmerov, Dmitry I. Pikulin, and Ion Cosma Fulga, Topological phases without crystalline counterparts, Phys. Rev. Lett. **123**, 196401 (2019).

[35] Rui Chen, Chui-Zhen Chen, Jin-Hua Gao, Bin Zhou, and Dong-Hui Xu, Higher-order topological insulators in quasicrystals, Phys. Rev. Lett. **124**, 036803 (2020).

[36] Di Zhou, Leyou Zhang, and Xiaoming Mao, Topological boundary floppy modes in quasicrystals, Phys. Rev. X **9**, 021054 (2019).

[37] Charles L. Kane and Tom C. Lubensky, Topological boundary modes in isostatic lattices, Nat. Phys. **10**, 39 (2014).

[38] Charles L. Kane and Eugene J. Mele, Quantum spin Hall effect in graphene, Phys. Rev. Lett. **95**, 226801 (2005).

[39] Huaqing Huang and Feng Liu, Quantum spin Hall effect and spin Bott index in a quasicrystal lattice, Phys. Rev. Lett. **121**, 126401 (2018).

[40] Huaqing Huang and Feng Liu, Theory of spin Bott index for quantum spin Hall states in nonperiodic systems, Phys. Rev. B **98**, 125130 (2018).

[41] Roman Süsstrunk and Sebastian D. Huber, Observation of phononic helical edge states in a mechanical topological insulator, Science **349**, 47 (2015).

[42] S. Hossein Mousavi, Alexander B. Khanikaev, and Zheng Wang, Topologically protected elastic waves in phononic metamaterials, Nat. Commun. **6**, 8682 (2015).

[43] Cheng He, Xu Ni, Hao Ge, Xiao-Chen Sun, Yan-Bin Chen, Ming-Hui Lu, Xiao-Ping Liu, and Yan-Feng Chen, Acoustic topological insulator and robust one-way sound transport, Nat. Phys. **12**, 1124 (2016).

[44] Rajesh Chaunsali, Chun-Wei Chen, and Jinkyu Yang, Subwavelength and directional control of flexural waves in zone-folding induced topological plates, Phys. Rev. B **97**, 054307 (2018).

[45] Marco Miniaci, R. K. Pal, B. Morvan, and M. Ruzzene, Experimental observation of topologically protected helical edge modes in patterned elastic plates, Phys. Rev. X **8**, 031074 (2018).

[46] Di Xiao, Wang Yao, and Qian Niu, Valley-contrasting physics in graphene: Magnetic moment and topological transport, Phys. Rev. Lett. **99**, 236809 (2007).

[47] Alexis Drouot and M. I. Weinstein, Edge states and the valley Hall effect, Adv. Math. **368**, 107142 (2020).

[48] Tzuhsuan Ma and Gennady Shvets, All-Si valley-Hall photonic topological insulator, New J. Phys. **18**, 025012 (2016).

[49] Jiho Noh, Sheng Huang, Kevin P. Chen, and Mikael C. Rechtsman, Observation of photonic topological valley Hall edge states, Phys. Rev. Lett. **120**, 063902 (2018).

[50] Jiuyang Lu, Chunyin Qiu, Liping Ye, Xiying Fan, Manzhu Ke, Fan Zhang, and Zhengyou Liu, Observation of topological valley transport of sound in sonic crystals, Nat. Phys. **13**, 369 (2017).

[51] Daniel Torrent, Didier Mayou, and José Sánchez-Dehesa, Elastic analog of graphene: Dirac cones and edge states for flexural waves in thin plates, Phys. Rev. B **87**, 115143 (2013).

[52] Javier Vila, Raj Kumar Pal, and Massimo Ruzzene, Observation of topological valley modes in an elastic hexagonal lattice, Phys. Rev. B **96**, 134307 (2017).

[53] Kai Qian, David J. Apigo, Camelia Prodan, Yafis Barlas, and Emil Prodan, Topology of the valley-Chern effect, Phys. Rev. B **98**, 155138 (2018).

[54] Yuning Guo, Matheus Inguaggiato Nora Rosa, Mohit Gupta, Benjamin Emerson Dolan, Brandon Fields, Lorenzo Valdevit, and Massimo Ruzzene, Minimal surface-based materials for topological elastic wave guiding, Adv. Funct. Mater. **32**, 2204122 (2022).

[55] Raj Kumar Pal and Massimo Ruzzene, Edge waves in plates with resonators: An elastic analogue of the quantum valley Hall effect, New J. Phys. **19**, 025001 (2017).

[56] Bryn Davies and Richard V. Craster, Symmetry-induced quasicrystalline waveguides, Wave Motion **115**, 103068 (2022).

[57] T. C. Lubensky, Chapter 6 - symmetry, elasticity, and hydrodynamics in quasiperiodic structures. In Marko V. Jarić, editor, *Introduction to Quasicrystals*, volume 1 of *Aperiodicity and Order* (Elsevier, San Diego, 1988), p. 199.

[58] M. Widom, Discussion of phasons in quasicrystals and their dynamics, Philosophical Magazine **88**, 2339 (2008).

[59] Danilo Beli, Matheus Inguaggiato Nora Rosa, Carlos De Marqui, and Massimo Ruzzene, Mechanics and dynamics of two-dimensional quasicrystalline composites, Extreme Mech. Lett. **44**, 101220 (2021).

[60] Danilo Beli, Matheus Inguaggiato Nora Rosa, Carlos De Marqui, and Massimo Ruzzene, Wave beaming and diffraction in quasicrystalline elastic metamaterial plates, Phys. Rev. Res. **4**, 043030 (2022).

[61] Yiquan Wang, Xiaoyong Hu, Xingsheng Xu, Bingying Cheng, and Daozhong Zhang, Localized modes in defect-free dodecagonal quasiperiodic photonic crystals, Phys. Rev. B **68**, 165106 (2003).

[62] Alessandro Della Villa, Stefan Enoch, Gérard Tayeb, Filippo Capolino, Vincenzo Pierro, and Vincenzo Galdi, Localized modes in photonic quasicrystals with Penrose-type lattice, Opt. Express **14**, 10021 (2006).

[63] Khaled Mnaymneh and Robert C. Gauthier, Mode localization and band-gap formation in defect-free photonic quasicrystals, Opt. Express **15**, 5089 (2007).

[64] Artem D. Sinelnik, Ivan I. Shishkin, Xiaochang Yu, Kirill B. Samusev, Pavel A. Belov, Mikhail F. Limonov, Pavel Ginzburg, and Mikhail V. Rybin, Experimental observation of intrinsic light localization in photonic icosahedral quasicrystals, Adv. Opt. Mater. **8**, 2001170 (2020).

[65] See Supplemental Material at http://link.aps.org/supplemental/10.1103/PhysRevApplied.23.024039 for an animation file showing the experimental transient response of the interface state in an additive manufactured quasicrystal.

[66] Yabin Jin, Daniel Torrent, and Bahram Djafari-Rouhani, Robustness of conventional and topologically protected edge states in phononic crystal plates, Phys. Rev. B **98**, 054307 (2018).

[67] Bakhtiyar Orazbayev and Romain Fleury, Quantitative robustness analysis of topological edge modes in c6 and valley-Hall metamaterial waveguides, Nanophotonics **8**, 1433 (2019).

[68] Guillermo Arregui, Jordi Gomis-Bresco, Clivia M. Sotomayor-Torres, and Pedro David Garcia, Quantifying the robustness of topological slow light, Phys. Rev. Lett. **126**, 027403 (2021).

[69] Yasuhiro Hatsugai, Chern number and edge states in the integer quantum Hall effect, Phys. Rev. Lett. **71**, 3697 (1993).

[70] Takahiro Fukui, Yasuhiro Hatsugai, and Hiroshi Suzuki, Chern numbers in discretized Brillouin zone: Efficient method of computing (spin) Hall conductances, J. Phys. Soc. Jpn. **74**, 1674 (2005).

[71] Peng Wang, Qidong Fu, Vladimir V. Konotop, Yaroslav V. Kartashov, and Fangwei Ye, Observation of localization of light in linear photonic quasicrystals with diverse rotational symmetries, Nat. Photonics **18**, 224 (2024).